International Journal of Heat and Mass Transfer 85 (2015) 265–280

Contents lists available at ScienceDirect

International Journal of Heat and Mass Transfer

journal homepage: www.elsevier.com/locate/ijhmt

Experimental and computational investigation of interfacial shear along a wavy two-phase interface

Nikhin Mascarenhas, Hyoungsoon Lee, Issam Mudawar *

Purdue University Boiling and Two-Phase Flow Laboratory (PU-BTPFL), School of Mechanical Engineering, 585 Purdue Mall, West Lafayette, IN 47907, USA

ARTICLE INFO

Article history:
Received 21 June 2014
Received in revised form 19 January 2015
Accepted 20 January 2015
Available online 16 February 2015

Keywords:
Interfacial waves
Interfacial viscous drag
Interfacial form drag
Eddy diffusivity

ABSTRACT

This study explores the complex fluid flow behavior adjacent to the interface between parallel layers of gas and liquid. Using water and nitrogen as working fluids, the interface is examined experimentally using high-speed video, and the flow structure predicted using FLUENT. The computational model is used to analyze the gas flow near the interface by isolating and examining a domain that represents an instantaneous snapshot of the wavy interface. Both the observed and computed interfaces show appreciable interfacial waviness, which increases in intensity with increasing flow rates; they also show gas entrainment effects at high flow rates. The computed results show turbulence is completely suppressed along the interface by surface tension. Computed velocity vector plots, contour plots and flow streamlines show interfacial flow separation on the gas side, and these effects are amplified with increasing gas Reynolds number. This produces form drag along the wavy interface in addition to the viscous drag. The interfacial viscous and form drag components increase monotonically with increasing ratio of wave height to wavelength because of the increased frictional resistance and flow separation effects, respectively. A new relation for the interfacial friction factor is derived from the computational results, which agrees well with prior turbulent flow correlations.

1. Introduction

Two-phase flow models incorporate several transport parameters that are represented in terms of fluid properties, flow rates and length scales. However, these models are further complicated by interfacial traits that are not easily predicted. The interfacial wave structure and interfacial dampening of turbulent eddies have been the focus of considerable study [1–3]. These, in turn, influence interfacial velocity and temperature gradient, key ingredients in the development of relations for interfacial mass transfer, shear and heat flux found in theoretical two-phase flow models. The dynamics of fluid flow along turbulent interfaces needs to be investigated in order to resolve the inter-dependent nature of these interfacial parameters.

Interfacial shear can be neglected in the case of free-falling films [4,5]. Where interfacial shear is significant, empirical expressions are incorporated into two-phase models with varying degrees of difficulty, such as the homogeneous equilibrium model and slip-flow model. Empirical relations for interfacial shear aim to account for interfacial momentum transfer due to evaporation or condensation [6], as well as interfacial waviness [6–8]. The pursuit of an improved model for interfacial shear requires systematic assessment of key transport parameters of a turbulent wavy interface, such as both shear and drag forces, eddy diffusivity and length scales associated with a wavy interface.

1.1. Interfacial drag

An examination of literature on the fluid dynamics of two-phase flows shows a far greater focus on interfacial shear as compared to interfacial drag. Ishii and Zuber [9] constructed a unified law for drag coefficient in dispersed flows. Kataoka et al. [10] developed an expression for the interfacial drag coefficient in annular flow, which they used to predict droplet entrainment parameters. Because of the large differences between gas and liquid velocities in annular flow, it is useful to examine drag effects for gas flow along a wavy solid surface. Salvetti et al. [11] studied drag forces exerted along solid sinusoidal surfaces, and consolidated measured and simulated findings from previous studies. Their parametric study considered flow rate, fluid properties and surface profile as salient variables that influence the drag coefficient.

1.2. Interfacial shear in annular two-phase flow

Hartley and Roberts [12] were among the first investigators to recommend a relationship between interfacial friction coefficient,

* Corresponding author. Tel.: +1 765 494 5705; fax: +1 765 494 0539.
E-mail address: mudawar@ecn.purdue.edu (I. Mudawar).
URL: https://engineering.purdue.edu/BTPFL (I. Mudawar).

http://dx.doi.org/10.1016/j.ijheatmasstransfer.2015.01.096
0017-9310/

Nomenclature

A	local projected interfacial area
C_D	combined (viscous plus form) drag coefficient
$C_{f,D}$	coefficient of viscous drag
$C_{f,i}$	interfacial skin friction coefficient
C_p'	canonical pressure distribution
$C_{\varepsilon 1}$, $C_{\varepsilon 2}$	constants in turbulent kinetic energy transport equation
C_μ	constants in Boussinesq equation
D	hydraulic diameter of entire channel
D_H	hydraulic diameter of liquid layer
$\hat{e}_d$	unit vector parallel to flow direction
$F_{D,form}$	form drag
$F_{D,visv}$	viscous drag
f_g	wall friction factor for Domain 2
f_i	interfacial friction factor
g	gravitational acceleration
h	interfacial wave height
k	turbulent kinetic energy, constant in Stratford [43] separation theory
l	interfacial wavelength
N	number of discrete data points
n	number of samples in subset of data record
$\hat{n}$	unit vector normal to interface
P	pressure; probability
p	probability density
Re	Reynolds number
S	area of curved interface
t	time
$\hat{t}$	unit vector parallel to interface
U	inlet mean x-direction velocity
u_x	x-direction velocity component
$\bar{u}_{x,m}$	local x-direction velocity component averaged over y-span at same location
u_y	y-direction velocity component
u_z	z-direction velocity component
V	inlet y-direction velocity
W	inlet z-direction velocity
x, y, z	spatial coordinates
x'	effective boundary layer length

Greek symbols

δ	annular film thickness
ε	dissipation rate of turbulent kinetic energy
ε_m	eddy momentum diffusivity
μ	dynamic viscosity
ν	kinematic viscosity
ω	turbulent specific dissipation
ρ	density
σ_κ	constant in turbulent kinetic energy transport equation
σ_ε	constant in turbulent dissipation transport equation
τ	shear stress

Subscripts

form	form or pressure (drag)
g	gas
i	interface
l	liquid, laminar
max	maximum
t	turbulent
visc	viscous (drag)
w	wall

Superscripts

$-$	mean component; average
+	non-dimensional
$'$	fluctuating component

f_i, and dimensionless film thickness in annular two-phase flow. Wallis [6] developed a theoretical model for interfacial shear, τ_i, in annular flow in terms of flow rate and fluid properties. His model incorporated the influence of drag forces by modifying an expression by Silver and Wallis [13] based on the Reynolds flux concept. Wallis [14,15] later published at a curve fit for f_i that yielded good agreement with pressure drop data for annular flow. Henstock and Hanratty [16] studied air–water annular flow assuming a known entrainment rate, and correlated interfacial shear to the mass flow rate. Using an extensive experimental database, Kataoka et al. [10] updated the Wallis correlation [14] to account for interfacial wave amplitude, which they expressed in terms of f_i and fluid properties. Asali et al. [17] improved this correlation for vertical annular flows by employing an updated technique for measuring annular film thickness in the presence of droplet entrainment.

Narain et al. [18] studied annular condensing flows at different inclinations and proposed an asymptotic model for τ_i that showed good agreement with data. Other published models for τ_i include those of Mickley [19], Shekriladze and Gomelauri [20], Moeck [21], Andreussi [22], Soliman et al. [23], and Spedding and Hand [24]. Fukano and Furukawa [25] investigated the influence of liquid viscosity on interfacial shear in vertical annular upflow, and recommended a correlation for τ_i in terms of f_i and fluid properties. Their unconventional formulation involved higher order terms that accounted for the significant increase in interfacial drag for large film thicknesses. Fore et al. [26] performed experiments involving vertical annular concurrent flow of water and nitrogen to broaden the application range of the Wallis [14] correlation. Their expression demarcated the behavior of f_i at medium and high flow rates, as opposed to the uniform treatment of Wallis [15]. Using a large database and focusing on thick annular films, Wongwises and Kongkiatwanitch [27] recommended yet another correlation for f_i, which accounted for roughness effects over a wider range of flow rates. A common thread observed in all these models is their inability to demarcate the entrainment effects due to phase change from those due to fluid dynamics.

The present study concerns the interfacial characteristics and fluid dynamics of adiabatic horizontal flow of a water film that is shear driven by a nitrogen stream. A facility is constructed to generate a nearly two-dimensional water film whose interface could be captured using high-speed video imaging. Using FLUENT, a computational model is constructed to generate interfacial shape (profile), whose wavy features and turbulence effects are carefully examined. The liquid velocity and interfacial shear stress are inspected to gain detailed insight into their three-dimensional distributions in terms interfacial profile. Skin friction distribution and gas flow separation effects are also examined. A relation is derived for the interfacial friction factor as a function of both liquid film thickness and ratio of wave height to wavelength. Also proposed are relations for the drag coefficient, which can be used to derive criteria for droplet entrainment.

2. Experimental facility

An experimental facility is constructed to study the interfacial structure of horizontal adiabatic water–nitrogen flow. The facility

is comprised of a fluid delivery system, test section and video imaging system. Fig. 1(a) shows a schematic of the fluid delivery system, which is designed to deliver de-ionized water and nitrogen gas to the test module at desired flow rates. The fluid delivery system consists of a water flow loop and a nitrogen gas flow loop. In the water loop, de-ionized water from a reservoir is pumped through a 5-μm filter followed by one of several flow meters connected in parallel, before entering the test section. In the nitrogen loop, nitrogen gas is supplied from a pressure cylinder and measured by one of several gas flow meters. The water merges with the nitrogen in the test section, and the mixture is returned to the reservoir, where the nitrogen is vented to the ambient.

Fig. 1(b) and (c) show, respectively, an exploded view and photo of the test section. This main component of the experimental facility consists of a transparent flow module consisting of a base plate, top plate and cover plate, all made from transparent acrylic to facilitate optical and visual access to the flow within the channel. The channel itself is a 6-mm wide and 2.5-mm deep slot that is machined into the lower base plate. The base plate contains deep plenums leading to shallow plenums at both channel ends. A flow divider is inserted in the inlet plenum and is designed to transport water and nitrogen from the inlet ports to the channel with minimum swirl. Made from Accura 60 resin, the divider is fabricated using a rapid prototyping process. The divider is fitted with a 0.1-mm aluminum precision machined barrier plate, the downstream end of which is sharpened gradually to ensure smooth merging of the two fluids. The 39-mm length of the barrier plate ensures that the flows of both fluids overcome any upstream swirl for all flow rates considered, leaving a downstream channel length of 81 mm for interaction between the two fluids. The rectangular flow channel is closed atop by the 1.6-mm thick channel cover plate. The entire assembly, including the base plate, top plate, channel cover plate, and flow divider, are pressed together and held firmly in place with the aid of two sets of aluminum clamps. The cover plate has a slot on its underside that acts as a seat to accommodate the barrier plate. Not shown in Fig. 1(b) is an O-ring that is pressed in a groove in the base plate to guard against any leaks between the base plate and channel cover plate. The test section is oriented to ensure that the nitrogen gas flows over the water. Fig. 1(d) shows a photo of the complete test facility.

Experiments are performed for liquid Reynolds numbers ranging from $Re_l = 400$ to 11,000 to cover both laminar and turbulent liquid conditions. The liquid–gas interface is captured with the aid of a Photron FASTCAM-Ultima high-speed video camera fitted with a Micro-Nikkor 105-mm f/2.8G lens. Video segments are recorded for up to 0.682 s at 500 frames per second (fps) with a pixel resolution of 1024 × 256. Lighting is provided by 16 of 5-W white LEDs that are fitted into a fan-cooled enclosure.

3. Computational methods

The fluid flow system considered is three-dimensional, unsteady, turbulent and adiabatic. It is modeled by solving the

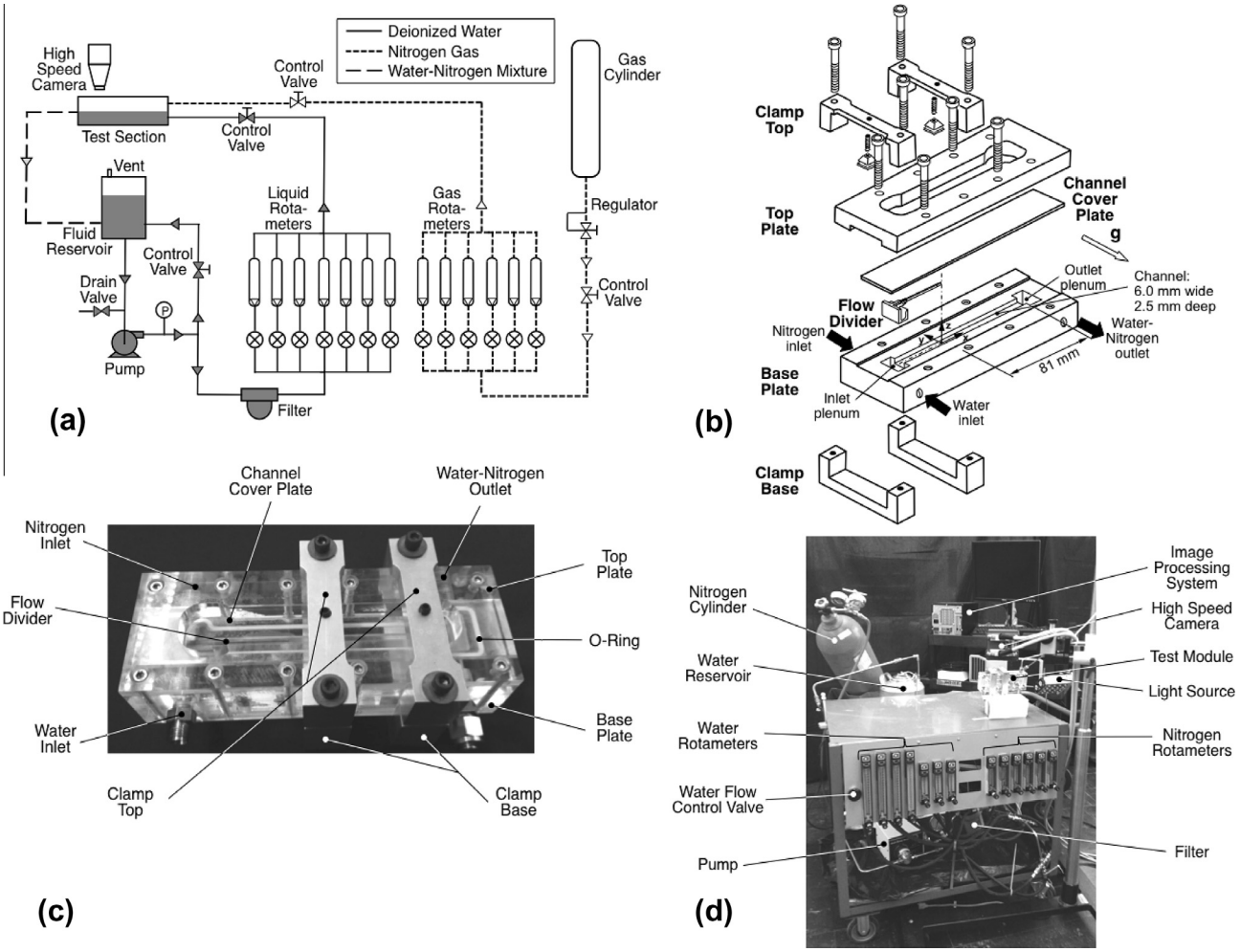

Fig. 1. (a) Schematic diagram of flow loop. (b) Exploded view of test section. (c) Photo of test section. (d) Photo of test facility.

three-dimensional unsteady Navier–Stokes equations in Cartesian coordinates. The mass and momentum equations are subjected to Reynolds decomposition [28], and time-averaged as [29]

$$\frac{\partial \bar{u}_x}{\partial x}+\frac{\partial \bar{u}_y}{\partial y}+\frac{\partial \bar{u}_z}{\partial z}=0, \tag{1}$$

$$\rho\left(\frac{\partial \bar{u}_x}{\partial t}+\bar{u}_x\frac{\partial \bar{u}_x}{\partial x}+\bar{u}_y\frac{\partial \bar{u}_x}{\partial y}+\bar{u}_z\frac{\partial \bar{u}_x}{\partial z}\right)=-\frac{\partial P}{\partial x}+\mu\left(\frac{\partial^2 \bar{u}_x}{\partial x^2}+\frac{\partial^2 \bar{u}_y}{\partial y^2}+\frac{\partial^2 \bar{u}_z}{\partial z^2}\right)+\rho\left(\frac{\partial}{\partial x}\left(-\langle u_x'^2\rangle\right)+\frac{\partial}{\partial x}\left(-\left\langle u_x'u_y'\right\rangle\right)+\frac{\partial}{\partial x}\left(-\langle u_x'u_z'\rangle\right)\right)+\rho g_x, \tag{2a}$$

$$\rho\left(\frac{\partial \bar{u}_y}{\partial t}+\bar{u}_x\frac{\partial \bar{u}_y}{\partial x}+\bar{u}_y\frac{\partial \bar{u}_y}{\partial y}+\bar{u}_z\frac{\partial \bar{u}_y}{\partial z}\right)=-\frac{\partial P}{\partial y}+\mu\left(\frac{\partial^2 \bar{u}_x}{\partial x^2}+\frac{\partial^2 \bar{u}_y}{\partial y^2}+\frac{\partial^2 \bar{u}_z}{\partial z^2}\right)+\rho\left(\frac{\partial}{\partial x}\left(-\langle u_y'u_x'\rangle\right)+\frac{\partial}{\partial y}\left(-\langle u_y'^2\rangle\right)+\frac{\partial}{\partial z}\left(-\langle u_y'u_z'\rangle\right)\right)+\rho g_y, \tag{2b}$$

and

$$\rho\left(\frac{\partial \bar{u}_z}{\partial t}+\bar{u}_x\frac{\partial \bar{u}_z}{\partial x}+\bar{u}_y\frac{\partial \bar{u}_z}{\partial y}+\bar{u}_z\frac{\partial \bar{u}_z}{\partial z}\right)=-\frac{\partial P}{\partial z}+\mu\left(\frac{\partial^2 \bar{u}_x}{\partial x^2}+\frac{\partial^2 \bar{u}_y}{\partial y^2}+\frac{\partial^2 \bar{u}_z}{\partial z^2}\right)+\rho\left(\frac{\partial}{\partial x}\left(-\langle u_z'u_x'\rangle\right)+\frac{\partial}{\partial y}\left(-\langle u_z'u_y'\rangle\right)+\frac{\partial}{\partial z}\left(-\langle u_z'^2\rangle\right)\right)+\rho g_z. \tag{2c}$$

Fig. 2 shows the two computational domains used in this study domains. Domain 1 represents the 81-mm long two-phase portion of the flow channel between the downstream edge of the barrier plate, where the two fluids begin to merge, to the downstream end of the channel. This domain allows the flow to establish a three-dimensional interface that is then exported to Domain 2. This second single-phase domain is used to explore the nitrogen flow alone along a wavy but stationary surface whose shape mimics that of the interface from Domain 1.

The boundary conditions for Domain 1 are specified as follows: at the inlet ($x = 0$), liquid velocity is assumed uniform and its magnitude based on the liquid Reynolds number, $U = \nu Re_1/D_H$, $V = 0$ and $W = 0$. The inlet velocity for nitrogen is prescribed in a similar manner, but adjusted to ensure that the interface is formed in the vicinity of $y = 3$ mm rather than shift towards the top or bottom walls of the channel. Fig. 3 shows, for each water Reynolds number, Re_l, the nitrogen Reynolds number, Re_g, that satisfies this interfacial criterion. Shown are clearly identifiable laminar and turbulent flow regimes based on the magnitude of Re_l. These regimes can be correlated according to the following relations.

$$\text{Laminar}: \quad \frac{\mathrm{Re}_g}{\mathrm{Re}_l}=14.42\mathrm{Re}_l^{-0.45}, \tag{3a}$$

$$\text{Turbulent}: \quad \frac{\mathrm{Re}_g}{\mathrm{Re}_l}=9.60\mathrm{Re}_l^{-0.31}. \tag{3b}$$

To resolve the turbulent terms in the governing equations, the k–ε two-equation model [29] is used. The $k-\varepsilon$ model provides closure to the turbulent stress terms by employing additional transport equations for turbulent kinetic energy, k, and its dissipation rate, ε, given respectively, by

$$\frac{\partial k}{\partial t}+\frac{\partial k\bar{u}_x}{\partial x}+\frac{\partial k\bar{u}_y}{\partial y}+\frac{\partial k\bar{u}_z}{\partial z}=-\langle u_x'^2\rangle\frac{\partial \bar{u}_x}{\partial x}-\langle u_x'u_y'\rangle\frac{\partial \bar{u}_x}{\partial y}-\langle u_x'u_z'\rangle\frac{\partial \bar{u}_x}{\partial z}-\langle u_y'u_x'\rangle\frac{\partial \bar{u}_y}{\partial x}-\langle u_y'^2\rangle\frac{\partial \bar{u}_y}{\partial y}-\langle u_y'u_z'\rangle\frac{\partial \bar{u}_y}{\partial z}-\langle u_z'u_x'\rangle\frac{\partial \bar{u}_z}{\partial x}-\langle u_z'u_y'\rangle\frac{\partial \bar{u}_z}{\partial y}-\langle u_z'^2\rangle\frac{\partial \bar{u}_z}{\partial z}-\varepsilon+\frac{\partial}{\partial x}\left\{\left(\frac{\varepsilon_m}{\sigma_k}+\nu\right)\frac{\partial k}{\partial x}\right\}+\frac{\partial}{\partial y}\left\{\left(\frac{\varepsilon_m}{\sigma_k}+\nu\right)\frac{\partial k}{\partial y}\right\}+\frac{\partial}{\partial z}\left\{\left(\frac{\varepsilon_m}{\sigma_k}+\nu\right)\frac{\partial k}{\partial z}\right\}, \tag{4a}$$

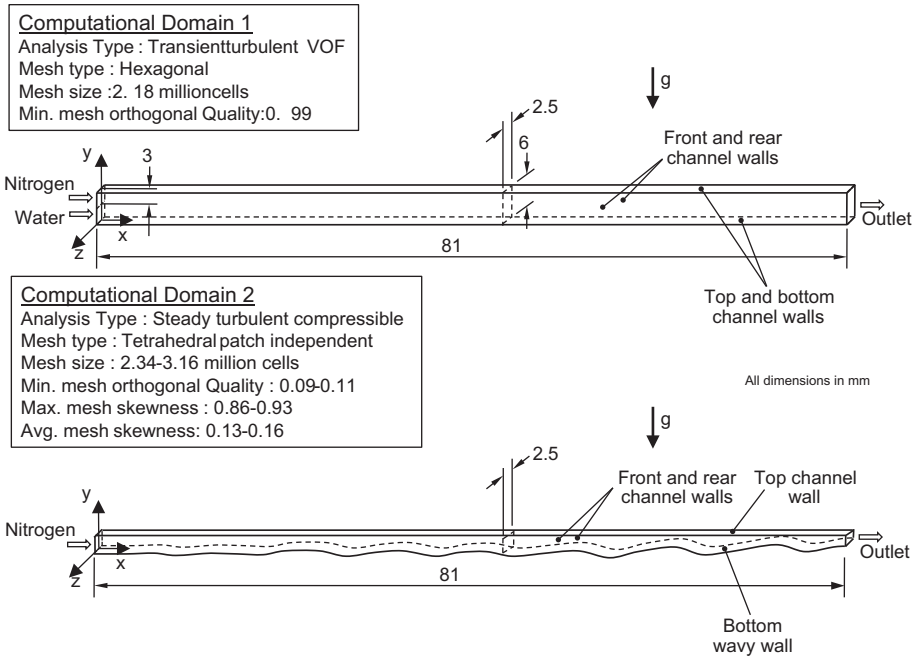

Fig. 2. Computational domains.

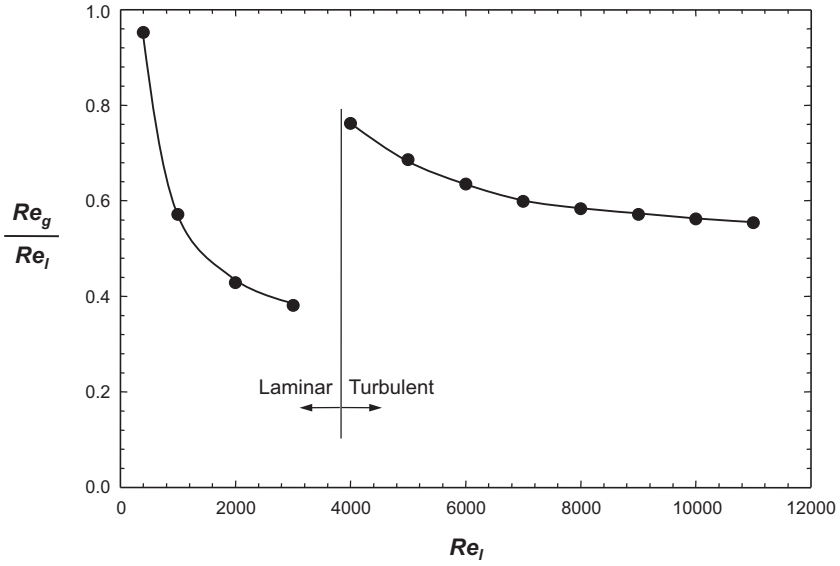

Fig. 3. Flow conditions for centerlined interface.

and

$$\frac{\partial \varepsilon}{\partial t}+\frac{\partial \varepsilon \bar{u}_x}{\partial x}+\frac{\partial \varepsilon \bar{u}_y}{\partial y}+\frac{\partial \varepsilon \bar{u}_z}{\partial z}=-C_{\varepsilon 1}\frac{\varepsilon}{k}\left(\langle u_x'^2\rangle\frac{\partial \bar{u}_x}{\partial x}+\langle u_x'u_y'\rangle\frac{\partial \bar{u}_x}{\partial y}+\langle u_x'u_z'\rangle\frac{\partial \bar{u}_x}{\partial z}+\langle u_y'u_x'\rangle\frac{\partial \bar{u}_y}{\partial x}+\langle u_y'^2\rangle\frac{\partial \bar{u}_y}{\partial y}+\langle u_y'u_z'\rangle\frac{\partial \bar{u}_y}{\partial z}\right)-C_{\varepsilon 1}\frac{\varepsilon}{k}\left(\langle u_z'u_x'\rangle\frac{\partial \bar{u}_z}{\partial x}+\langle u_z'u_y'\rangle\frac{\partial \bar{u}_z}{\partial y}+\langle u_z'^2\rangle\frac{\partial \bar{u}_z}{\partial z}\right)-C_{\varepsilon 2}\frac{\varepsilon^2}{k}+\frac{\partial}{\partial x}\left\{\left(\frac{\varepsilon_m}{\sigma_\varepsilon}+\nu\right)\frac{\partial \varepsilon}{\partial x}\right\}+\frac{\partial}{\partial y}\left\{\left(\frac{\varepsilon_m}{\sigma_\varepsilon}+\nu\right)\frac{\partial \varepsilon}{\partial y}\right\}+\frac{\partial}{\partial z}\left\{\left(\frac{\varepsilon_m}{\sigma_\varepsilon}+\nu\right)\frac{\partial \varepsilon}{\partial z}\right\}. \tag{4b}$$

Applying the Boussinesq eddy viscosity concept [29],

$$-\langle u_x'u_y'\rangle=\varepsilon_m\left(\frac{\partial \bar{u}_x}{\partial y}+\frac{\partial \bar{u}_y}{\partial x}\right), \tag{5a}$$

$$-\langle u_x'u_z'\rangle=\varepsilon_m\left(\frac{\partial \bar{u}_x}{\partial z}+\frac{\partial \bar{u}_z}{\partial x}\right), \tag{5b}$$

$$-\langle u_y'u_z'\rangle=\varepsilon_m\left(\frac{\partial \bar{u}_y}{\partial z}+\frac{\partial \bar{u}_z}{\partial y}\right), \tag{5c}$$

$$-\langle u_x'^2\rangle=2\varepsilon_m\frac{\partial \bar{u}_x}{\partial x}-\frac{2}{3}k, \tag{5d}$$

$$-\langle u_y'^2\rangle=2\varepsilon_m\frac{\partial \bar{u}_y}{\partial y}-\frac{2}{3}k, \tag{5e}$$

and

$$-\langle u_z'^2\rangle=2\varepsilon_m\frac{\partial \bar{u}_y}{\partial y}-\frac{2}{3}k, \tag{5f}$$

where

$$\varepsilon_m=C_\mu\frac{k^2}{\varepsilon}. \tag{6}$$

The present model utilizes standard values for all the constants in the above equations. For Domain 2, the k–ω model [30] is used because of its superior capability in addressing complex wall effects compared to the $k-\varepsilon$ model.

A recent study by the authors [3] points to the ability to extend FLUENT's flow modeling capability to tackle turbulent two-phase flows. In the present study, computations are performed using the FLUENT Analysis System in the Toolbox of ANSYS Workbench 14.0.0 [31]. The Project Schematic of Workbench in ANSYS FLUENT 14.5 is utilized to construct and mesh Domain 1. A User Defined Function (UDF) is written and applied to extract interfacial coordinates after steady state is attained, which are then rendered to form the volume that encompasses Domain 2. FLUENT is then used to perform the single-phase simulation for Domain 2. Overall, Domain 1 provides the interfacial profile and turbulent characteristics, and Domain 2 the interfacial stress and drag coefficient results.

At the interface in Domain 1, surface tension, molecular effects and gas shear effects are all considered. The model ensures that the tangential and normal force balance equations are always satisfied. To evaluate the local cell curvature, the volume fraction gradient is utilized in the continuum surface force model [32]. At the wall, wall adhesion in terms of the prescribed contact angle is taken to determine surface tension. The viscosity-influenced near-wall region is completely resolved all the way to the viscous sublayer, by demarcating this zone into a viscosity-influenced region and a fully turbulent region. In the fully turbulent region, the $k-\varepsilon$ model is employed to define turbulent viscosity, while the one-equation model of Wolfstein [33] is applied in the viscosity-influenced near-wall region; the length scale for turbulent viscosity in the latter is derived according to Chen and Patel [34]. The smooth blending of this multi-layer definition for turbulent viscosity with the high Reynolds number profile from the outer region is implemented as per [35]. Following [36], FLUENT then utilizes this two-layer model with a modified single function formulation of the law of the wall for the entire wall region, by blending laminar and turbulent law of the wall relations. This formulation ensures correct asymptotic behavior for large and small values of y^+ and suitable representation of velocity profiles where y^+ falls inside the buffer region.

For Domain 1, the two-phase treatment follows the Volume of Fluid (VOF) model [37]. In order to conserve computation time, the fractional step version of the non-iterative time advancement (NITA) scheme is used initially with first-order implicit discretization at every time step [38,39] to obtain pressure–velocity coupling. At convergence, third-order iterations are employed.

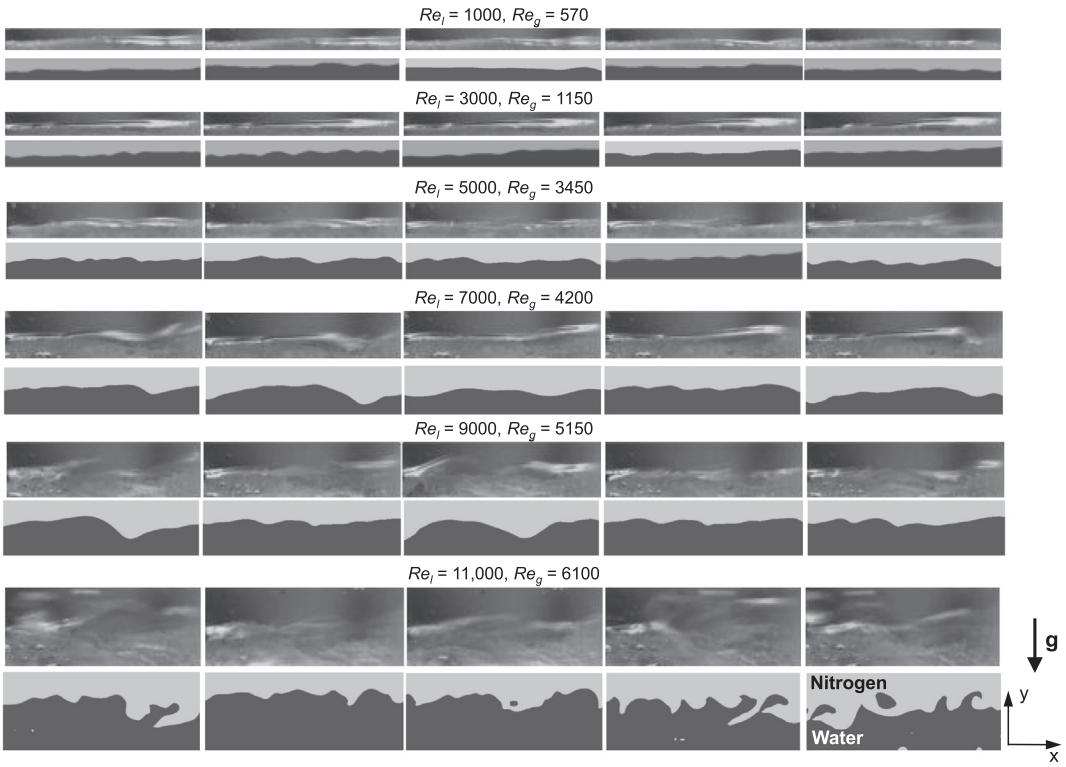

Fig. 4. Sequential images of water layer interface at $x = 54$ mm compared with corresponding computed interface plots for different water and nitrogen flow rates using Domain 1. Individual images in each sequence are 12-mm long and separated by 0.002 s.

Gradient generation during spatial discretization is accomplished using the least-squares cell-based scheme [40], while PRESTO, QUICK, Geo-reconstruct and first-order upwind schemes [41] are used for pressure, momentum, volume fraction and turbulent kinetic energy resolution, respectively.

Domain 2 is constructed as follows. The extracted interfacial coordinates are exported to a C-Sharp (C#) editor to collate the interfacial points in a readable format for commercial surface rendering software. MeshLab, product of Visual Computing Lab, is used to create the three-dimensional surface. Geomagic Studio, product of 3D Systems, is then used to remove surface inconsistencies. Afterwards, Blender 2.7 software is used to convert the surface into a volume by a sequential extrusion process that creates several internal self-intersections. Netfabb 5.0 is used to remove the self-intersections and supply the volume to Solidworks. In this final stage, the volume is converted to a format that can be recognized by ANSYS as a solid mesh. ANSYS FLUENT then performs a single-phase iterative steady state analysis on this volume.

Fig. 2 provides the grid size details for both domains, which are arrived at after careful assessment in pursuit of optimum degree of mesh refinement. This process involves evaluating the influence of mesh size on computational effort and quality of results. The grid system used is non-uniform, with a larger number of grid points near the walls and interface to achieve superior accuracy in resolving key flow parameters. It is important to note that the transition in refinement due to non-uniformity is gradual to avoid influencing the flow.

4. Flow visualization results

Fig. 4 shows the flow visualization results for a 12-mm segment of the flow channel centered at $x = 54$ mm for $Re_l = 1000$–$11{,}000$ and $Re_g = 570$–6100 per Fig. 3. Five sequential images, spaced 0.002 s apart, are presented for each combination of Re_l and Re_g to capture the transient behavior of the interface. Below each image is a corresponding computed interface plot. At $Re_l = 1000$ and $Re_g = 570$, the images and computed plots depict a relatively smooth interface with small amplitude waves. At $Re_l = 3000$ and $Re_g = 1150$, both the images and computed plots show an increase in the interfacial wave amplitude. At $Re_l = 5000$ and $Re_g = 3450$, the interface displays further increase in wave amplitude with a broader spectrum of wavelengths. For $Re_l = 7000$ and $Re_g = 4200$, and $Re_l = 9000$ and $Re_g = 5150$, there are further increases in wave amplitude along with nitrogen entrainment in the water layer. At $Re_l = 11{,}000$ and $Re_g = 6100$, the interface is marred by appreciable entrainment and deposition effects. The computed plots for this condition clearly capture the highly unstable interface and entrainment and deposition effects for this condition.

5. Computational results

5.1. Interfacial profile and Eddy diffusivity

Fig. 5 shows the shape of the interface at low, medium and high water Reynolds numbers. An inspection of these profiles is important, as they influence the degree of flow separation and frictional resistance exerted. As expected, an increase in flow rate causes the interface to be subjected to greater shear, but the input parameters maintain the sheared interface at the mid-plane. The interface is clearly three-dimensional with a discernable pattern in the z direction. The disturbances are most prominent at the walls, and decrease in intensity towards the central plane, a consequence of the velocity gradient induced by the near wall effects.

The computed interfacial wave characteristics are examined in Fig. 6 with the aid of normalized probability density of the ratio of the wave height, h to wavelength, l, for all Re_l values considered. The normalized probability density, $p\ (h/l)$, is given by

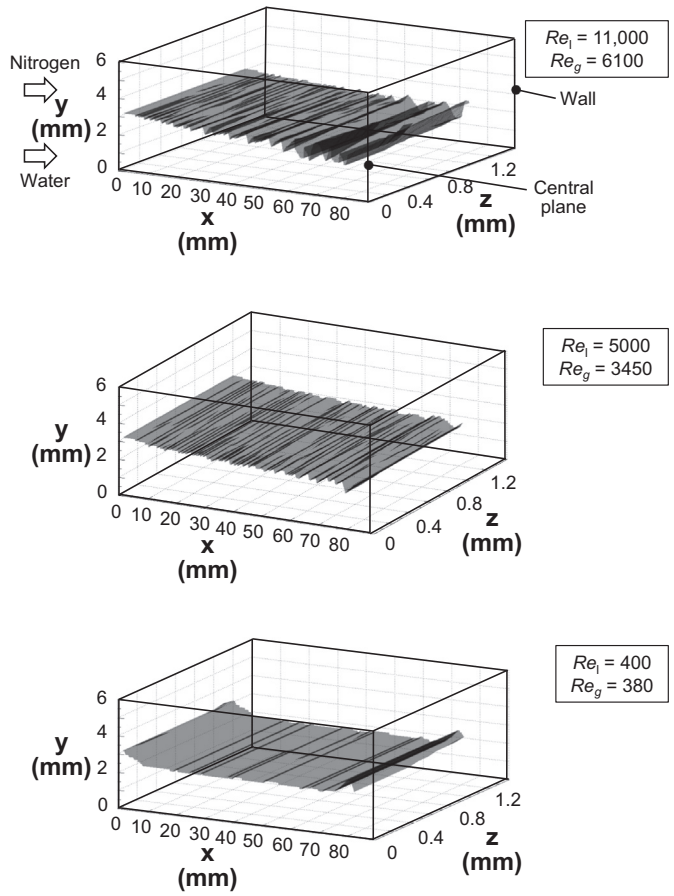

Fig. 5. Domain 1 computed interface plots for different flow rates.

$$p(h/l) = \frac{1}{\max\{p(h/l)\}}\left[\lim_{\Delta(h/l)\to 0}\frac{\mathrm{Prob}\{h/l < h/l(t) < h/l + \Delta(h/l)\}}{\Delta h/l}\right] = \frac{1}{\max\{p(h/l)\}}\frac{\mathrm{dP}(h/l)}{d(h/l)}, \tag{7}$$

where $P\,(h/l)$ is the probability distribution given by [42]

$$P(h/l) = \mathrm{Prob}\{h/l(t) < h/l\} = \frac{n\{h/l(t) < h/l\}}{N}. \tag{8}$$

Here, $P\,(h/l)$ describes the probability that the random variable, $h/l\,(t)$, will have a value less than or equal to a specified value, h/l, and N and n are the total number of time samples and number of time samples in a subset, respectively. The sampling is performed at $x = 54$ mm to ensure that the flow is unaffected by upstream or downstream effects. The total sampling time ranges from 0.1 s for $Re_l = 400$ to 0.01 s for $Re_l = 11{,}000$ in order to capture at least 10 waves.

Casting the interfacial characteristics in terms of probability density helps reduce the randomness in the data and eliminates noise due to any numerical instabilities. These statistically averaged characteristics are used later to develop relations for the interfacial stresses. Fig. 6 shows that the range of h/l increases with increasing Re_l, especially for $Re_l = 400$–5000. This can be attributed to the trend captured in Fig. 3, where Re_g/Re_l shows a significant decrease below $Re_l = 4000$. Notice in Fig. 6 that, because inertial effects are more balanced for $Re_l > 5000$, the increase in the h/l range is far smaller than for $Re_l = 400$–5000.

Fig. 7 shows the time-averaged eddy diffusivity profiles across the water layer for different Re_l and Re_g values. Notice that the turbulence is completely suppressed at the interface because of surface tension effects as suggested in [1], and the eddy diffusivity profile has a broader span and different slope near the interface as compared to falling films [2]. It is also seen that, for most of the cases considered, peak eddy diffusivity is nearly constant, but the eddy diffusivity profiles are more distinct at high y^+ values.

5.2. Interfacial fluid dynamics

At $Re_l = 11{,}000$ and $Re_g = 6100$, the mean inlet velocities for water and nitrogen are 6.23 and 32 m/s, respectively, and for $Re_l = 400$ and $Re_g = 380$, the mean inlet velocities are 0.27 and 2.0 m/s, respectively. This shows that, for all cases considered, the mean velocity of nitrogen is appreciably greater than that of water. This explains the usefulness of Domain 2 computations, where the interface is assumed stationary to examine nitrogen flow behavior along the interface. Fig. 8 shows the x-velocity for

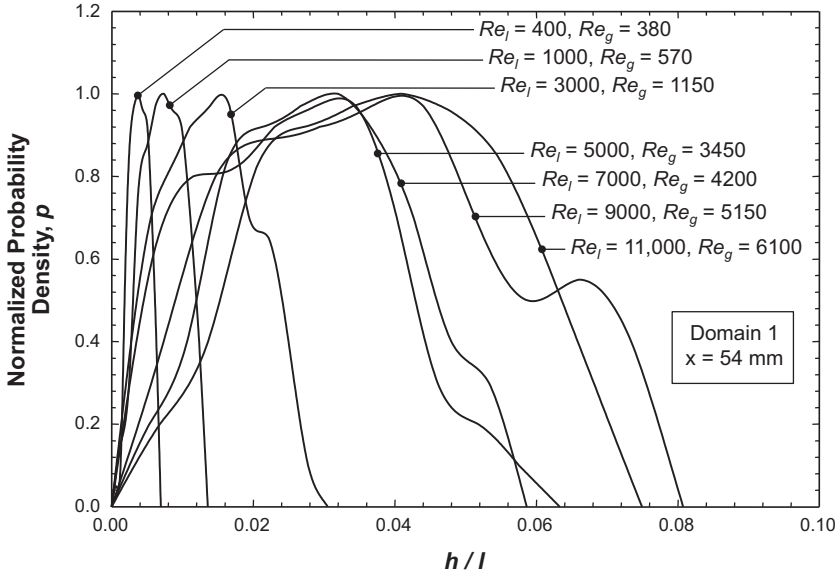

Fig. 6. Normalized probability density of h/l for different Re_l and Re_g values.

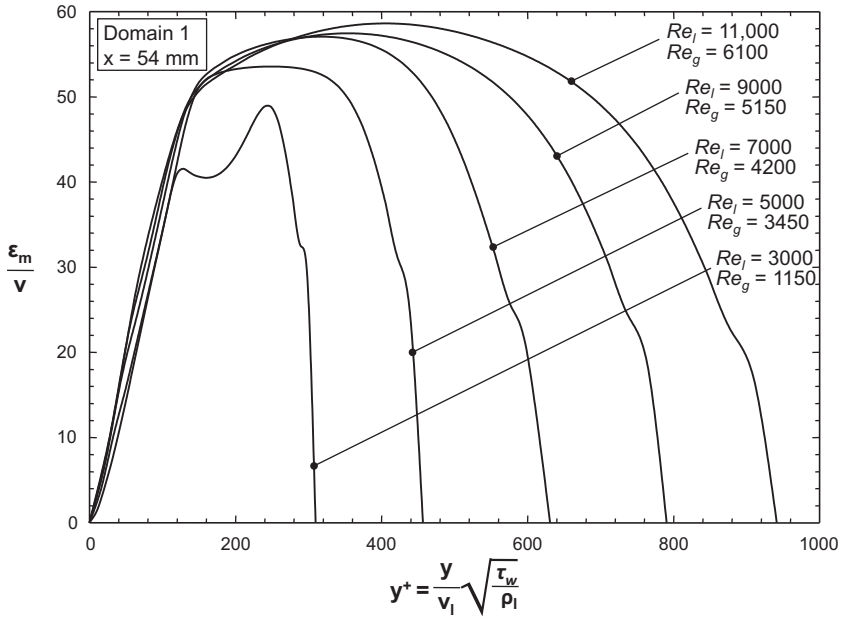

Fig. 7. Eddy diffusivity profiles across water layer for different Re_l and Re_g values.

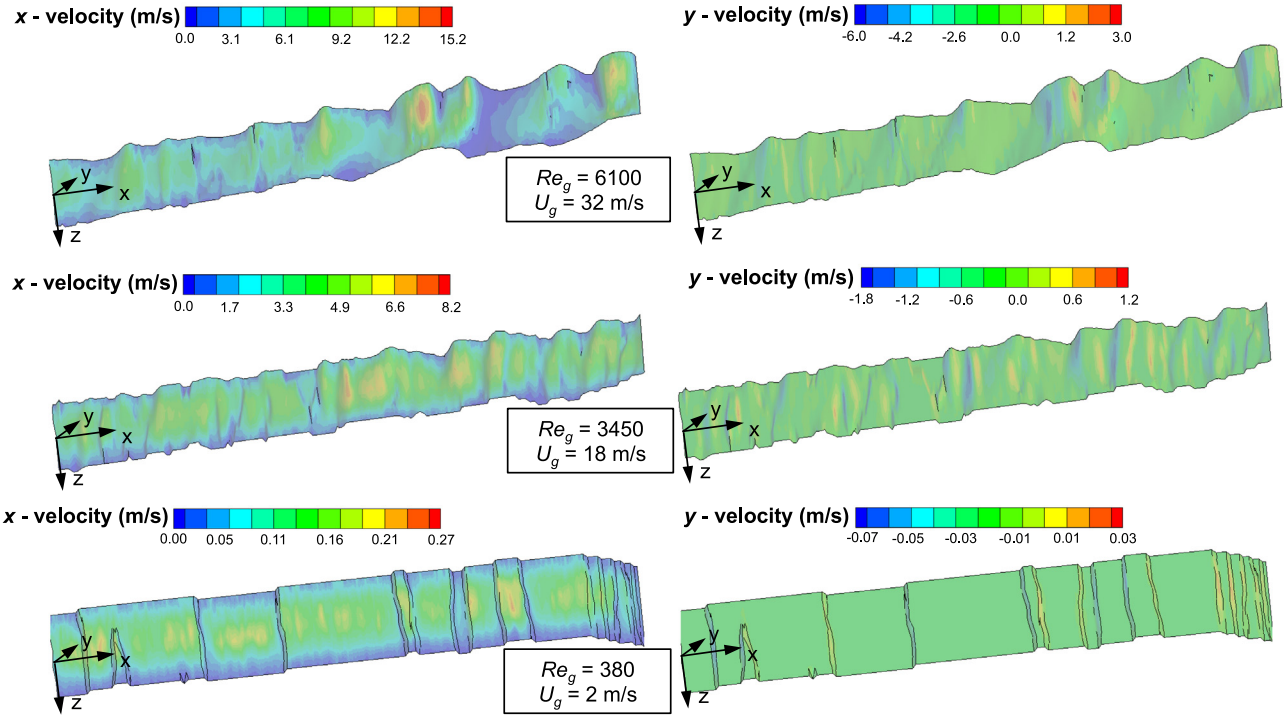

Fig. 8. Domain 2 (stationary interface) predictions of nitrogen *x*-velocity and *y*-velocity distributions along the interface for three operating conditions. The *y*-velocity is computed at 0.01 mm from the interface.

nitrogen flow along the curved but stationary interface (using Domain 2) at high, medium and low Re_g. Also shown is *y*-velocity at a small distance of 0.01 mm from the interface. For $Re_g = 6100$, the *x*-velocity is zero along the front and rear channel walls, highest along the crests of the large waves, and lowest in the deep troughs. For the same conditions, the *y*-velocity is expectedly appreciably smaller in magnitude than the *x*-velocity, and is highest in the advancing fronts of the large waves and lowest in the rear of the same waves. For $Re_g = 3450$, both the *x*-velocity and *y*-velocity are appreciably smaller than at $Re_g = 6100$, but show similar trends relative to the wave crests and troughs. At $Re_g = 380$, the *x*-velocity and *y*-velocity are comparatively quite small, and the interface far smoother than the other two cases, marred by few sharp curvature waves – ripples.

Fig. 9 shows Domain 2 nitrogen interfacial skin friction coefficient plots superimposed along the interface as well as projected from the interface for the same operating conditions as those in Fig. 8. The skin friction coefficient is defined as

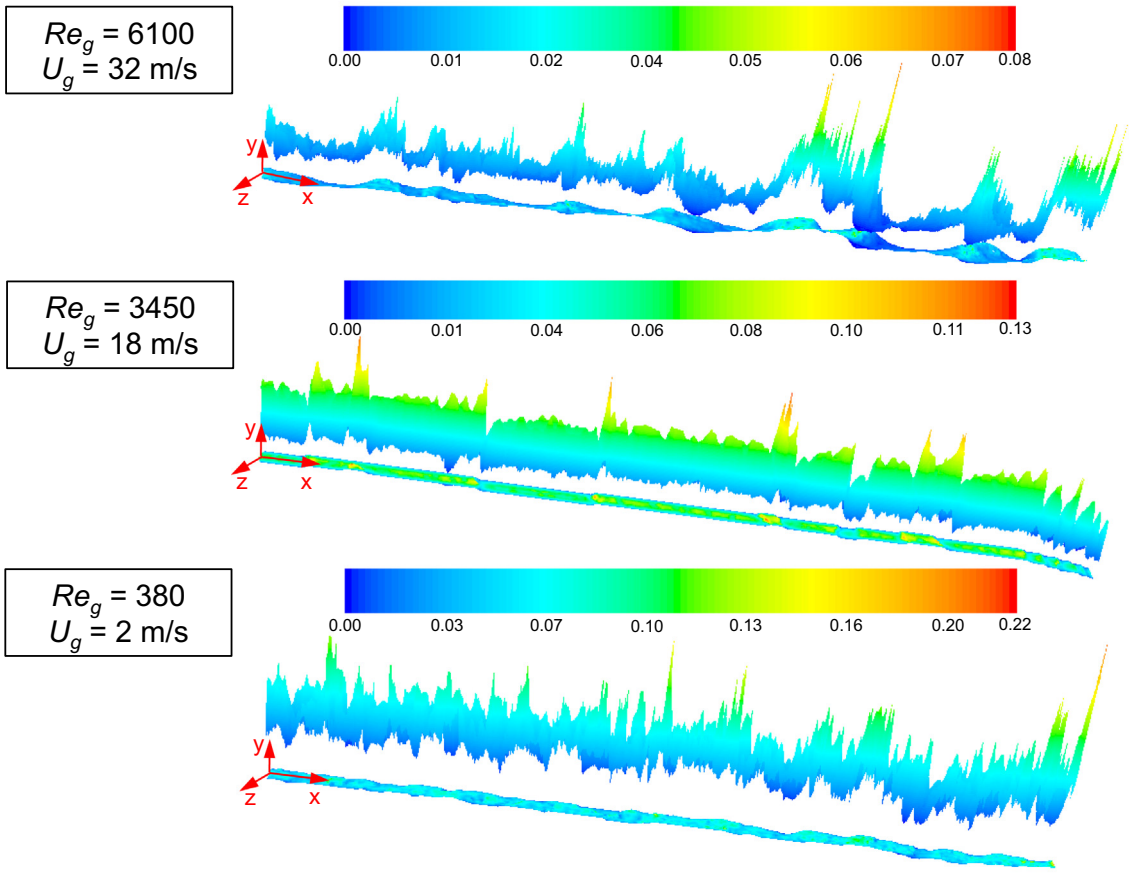

Fig. 9. Domain 2 (stationary interface) local nitrogen skin friction coefficient distributions, C_{fi}, for three operating conditions. Shown are skin friction coefficient plots superimposed along the interface as well as projected from the interface.

$$C_{f,i}(x,y,z) = \frac{\tau_i(x,y,z)}{\frac{1}{2}\rho_g u_{x,m}^2(x,z)}, \tag{9}$$

where τ_i is the interfacial shear and $u_{x,m}$ is the x-velocity at the corresponding x–z location in Domain 2 averaged over the y span, both computed using FLUENT. For Re_g = 6100, the interface exhibits several large waves, which are associated with skin friction coefficient values up to 0.08. For Re_g = 380, interfacial waviness is comparatively subdued but skin friction coefficient values are as large as 0.22.

Fig. 10 illustrates Domain 2 (stationary interface) computed separation effects in the nitrogen flow at highest and moderate Re_g numbers captured in velocity vector and velocity contour plots and in a streamline plot for the highest Re_g. The velocity vector and velocity contour plots are presented for the central plane (z = 0 mm). Notice in both the velocity vector and velocity contour plots, especially for Re_g = 3450, how the nitrogen impinges against the tail (left side) of the middle interfacial wave, and separates along the front (right side) of the same wave. This produces a net drag force upon the interfacial wave in addition to the shear force. The plots for Re_g = 6100 show appreciable swirl effects in the separation region, which is consistent with prior findings by the present authors concerning swirl effects in wavy, free-falling films [3]. These effects are also manifest in the streamline plot for Re_g = 6100, where the nitrogen streamlines are shown departing from the interface downstream from the waves. To better appreciate separation effects, the present results are compared to a criterion by Stratford [43] for turbulent flow separation along a convex surface,

$$C_p'\sqrt{x'\frac{dC_p'}{dx}} \leqslant k\left(\frac{\mathrm{Re}_{x'}}{10^6}\right)^{0.1}, \tag{10}$$

where

$$C_p' = 1 - \left(\frac{\bar{u}_x}{\bar{u}_{x,\max}}\right)^2, \tag{11}$$

$$x' = \int_0^{l/2}\left(\frac{\bar{u}_x}{\bar{u}_{x,\max}}\right)^3 dx + x - l/2. \tag{12}$$

$\bar{u}_{x,\max}$ is the maximum x-velocity at the corresponding x-location along the central plane in Domain 2, $\bar{u}_x$ is the x-velocity at the corresponding x-location along the central plane in Domain 2 averaged over the y-span, k = 0.35, and $l/2$ is the x-distance from the peak to the downstream edge of the surface. The surface in this criterion amounts to a single wave, however, the present study concerns a stationary interface with multiple waves. To apply his criterion to the present configuration, the coordinate x in Eq. (12) is set to zero at the start of every interfacial wave and $\overline{\mu}_{x,max}$ (maximum velocity associated with the same wave) is computed from the FLUENT model. This criterion predicts that separation will not occur for Re_g = 3450. However, as shown in Fig. 10, the present computations prove otherwise. It is not evident if the computed separation effects might be indication of the lack of applicability of the Stratford criterion for multiple waves, or the result of the k–ω model's tendency to generate excess separation [44].

5.3. Drag forces and coefficients

Fig. 11 shows Domain 2 (stationary interface) computed viscous and form drag forces for different h/l values. Viscous drag is the force exerted by the nitrogen on the stationary interface due to

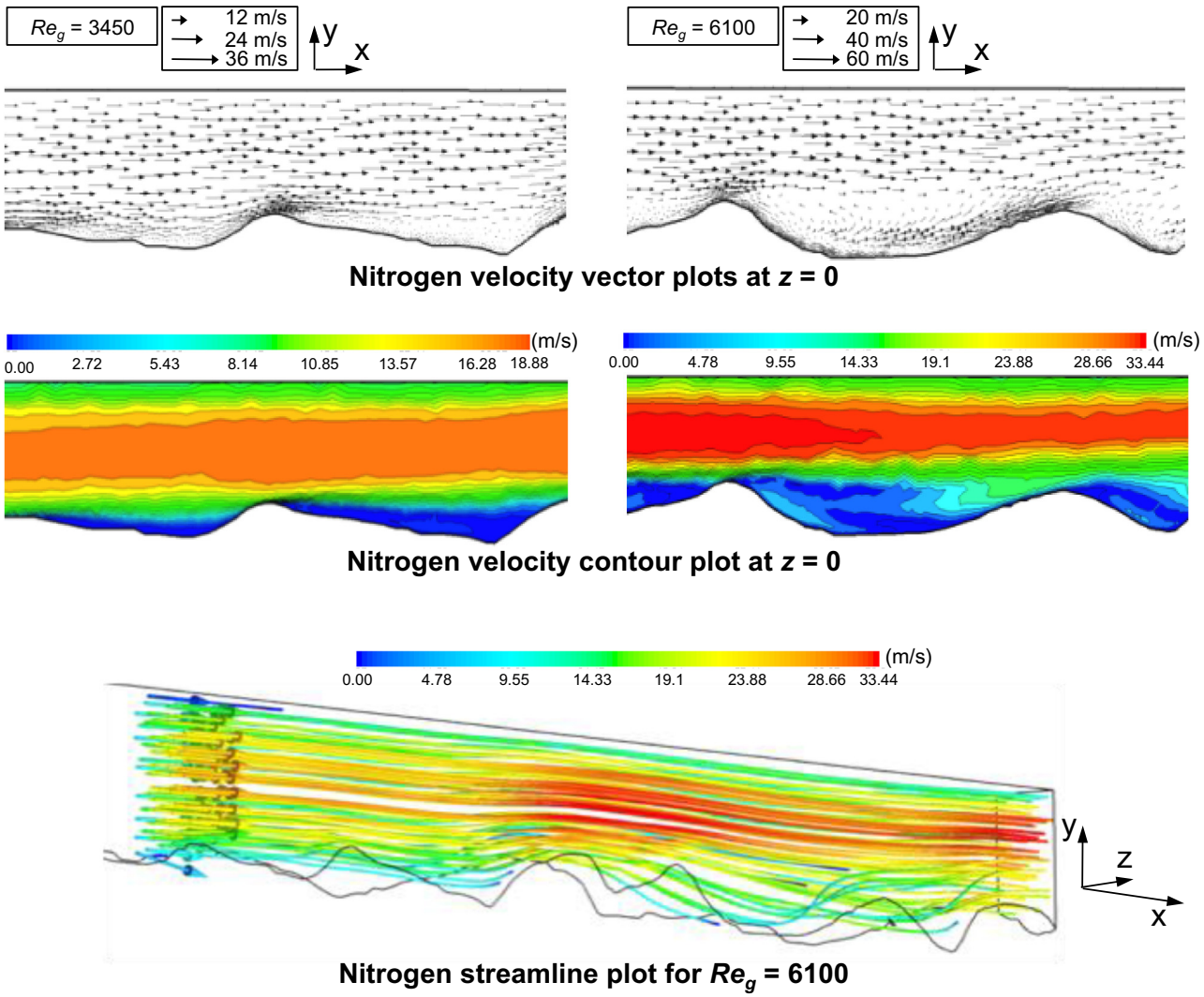

Fig. 10. Domain 2 (stationary interface) computed nitrogen velocity vector and contour plots along $z = 0$ (central plane) and $x = 54$ mm for two operating conditions, and streamline plot for highest Re_g and same axial location.

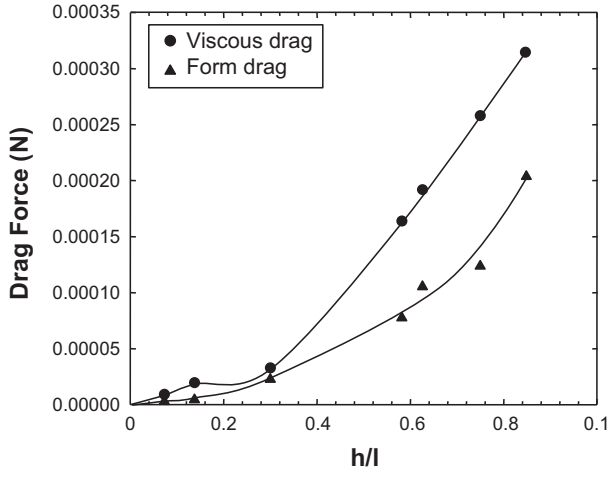

Fig. 11. Domain 2 (stationary interface) viscous and form drag force variations with h/l. The values of h/l used in this plot correspond to the largest values obtained from Fig. 6 for different combinations of Re_l and Re_g.

frictional resistance, and is calculated using the interfacial shear distribution as

$$F_{D,visc} = \int \tau_w \hat{t}.\hat{e}_d dS. \tag{13}$$

Here, τ_w is the local shear on the interface, $\hat{t}$ is the unit vector parallel to the interface, $\hat{e}_d$ is the unit vector parallel to the flow direction, and dS is the differential area of the curved interface. Form drag is the inertial force caused by separation of the boundary layer from the interface and the wake created by the separation, calculated from the pressure distribution as

$$F_{D,form} = \int P\hat{n}.\hat{e}_d dS. \tag{14}$$

Here, P is the local pressure and $\hat{n}$ the unit vector normal to the interface. The values of h/l used in Fig. 11 correspond to the largest values obtained from Fig. 6 for different combinations of Re_l and Re_g. The viscous and form drag forces are calculated by integrating the local drag components over the curved interfacial area, followed by dividing the integrated value over the area itself. Both forces

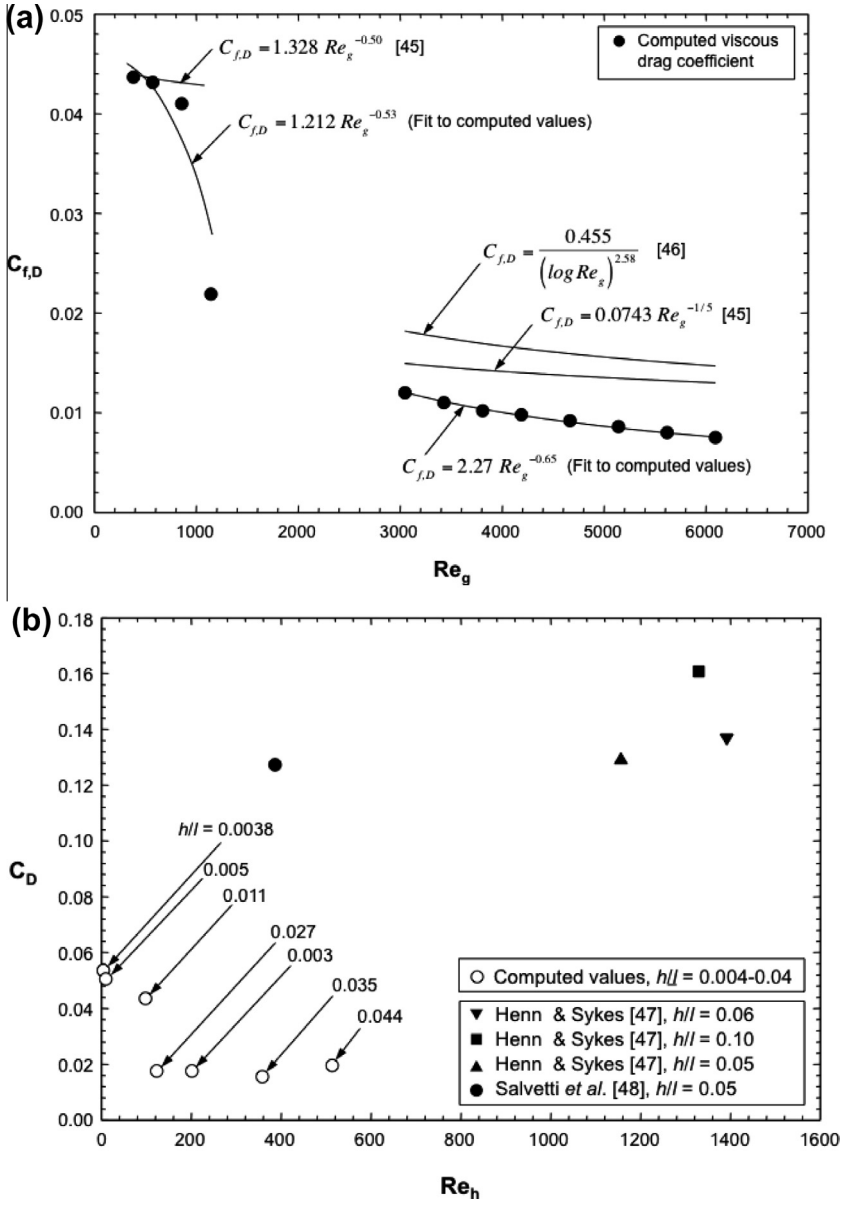

Fig. 12. (a) Computed Domain 2 (stationary interface) nitrogen viscous drag coefficient versus Re_g compared to prior laminar and turbulent correlations for flow over a flat surface. (b) Computed Domain 2 nitrogen drag coefficient versus Re_h compared to prior experimental correlations for flow over sinusoidal surfaces.

increase monotonically with increasing h/l. The viscous drag trend is attributed to the increase in wall friction since h/l increases with increasing Re_g, i.e., with increasing flow velocity. The discontinuity in the viscous drag force plot around $h/l = 0.3$ can be attributed to the transition between laminar and turbulent flows as depicted in Fig. 3. The form drag increases with increased angle of attack; it is negligible for very small values of h/l and becomes important for $h/l > 0.4$, where separation effects become significant.

Fig. 12(a) shows Domain 2 computed and fitted viscous drag coefficients versus Re_g, along with prior experimental correlations for viscous drag for flat surfaces. The viscous drag coefficient is a dimensionless measure of the viscous drag, defined as

$$C_{f,D} = \frac{F_{d,visc}/A}{\frac{1}{2}\rho_g U^2}, \tag{15}$$

where A is the flat projected interfacial area and U is the mean inlet x-direction velocity. The computed laminar and turbulent viscous drag friction coefficients are fitted according to the following relations:

$$\text{Laminar}: \quad C_{f,D} = 1.212\text{Re}_g^{-0.53}, \tag{16a}$$

$$\text{Turbulent}: \quad C_{f,D} = 2.27\text{Re}_g^{-0.65}. \tag{16b}$$

Overall, the inverse dependence of the viscous drag coefficient on Re_g is consistent with the trends of prior correlations. There is better agreement in magnitude with correlations for the turbulent region [45,46]. The predictions do not compare well in the laminar region. The differences between computed and experimental trends can be attributed to the curvature effects, which are not accounted for in flat plate correlations.

Fig. 12(b) shows Domain 2 computed and fitted combined drag coefficients versus Re_g along with prior experimental correlations for flow over sinusoidal surfaces [47,48]. The combined drag coefficient is a dimensionless measure of the combined effect of the viscous and form drag, defined as

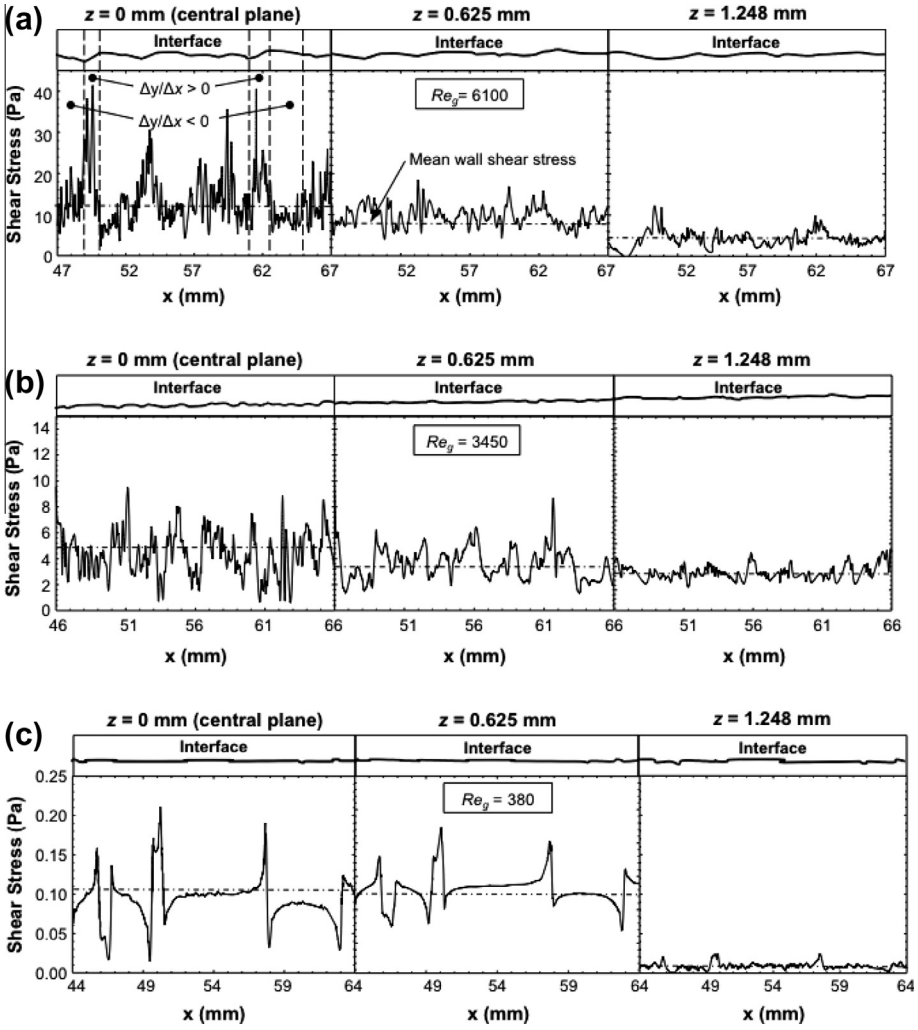

Fig. 13. Computed Domain 2 (stationary interface) nitrogen shear stress distributions for (a) Re_g 6100, (b) Re_g = 3450, and (c) Re_g = 380.

$$C_D = \frac{F_D/A}{\frac{1}{2}\rho_g u_{x,m}^2}. \tag{17}$$

It is apparent that the predictions are well below those for sinusoidal surfaces. Differences can be attributed to several factors. First, the h/l range considered is lower than h/l available for comparison. Second, the h/l range for the present conditions is not consistently maintained over the entire interface. Third, the present interfacial profiles are not sinusoidal, and their angle of attack is therefore considerably different.

5.4. Interfacial shear stress

Fig. 13(a)–(c) show distributions of interfacial shear stress for Re_g = 6100, 3450 and 380, respectively, which accounts for viscous and form drag combined. Shown in each figure are the shear stress and interface profile at z = 0 (central plane), 0.625 and 1.248 mm. For the case of Re_g = 6100, where the interfacial undulation is pronounced, additional shear characteristics are highlighted. These plots show the shear stress decreases in the wave fronts, because of boundary layer separation effects, and increases in the wave tails because of stronger boundary layer attachment in these regions. In the presence of separation, these wave front and wave tail differences both increase form drag on the wave and viscous drag on the tail. These trends are not easily discernable at the lower flow rates, where the interfacial wave structure is less pronounced. Fig. 13(a)–(c) show the interfacial shear stress increases with increases in flow rate and/or distance from the wall. Notice in Fig. 13(c) the significant reduction in the magnitude of interfacial shear at z = 1.248 mm compared to z locations at or closer to the centerline. This can be explained by the thicker wall boundary layer at this low Reynolds number.

In order to derive an estimate of mean interfacial shear stress over the portion of the interface spanning the entire z-direction width and x-direction range indicated in Fig. 13(a)–(c), the local interfacial shear stress is integrated and averaged over the same area. For comparison, shear is calculated using the popular semi-empirical correlation by Wallis [6]

$$\tau_i(x,z) = \frac{1}{2} f_i \rho_g [u_{x,m}(x,z) - u_i(x,z)]^2. \tag{18}$$

For turbulent flow, the interfacial friction factor, f_i, is replaced by the expression [14]

$$f_{i,t} = f_g \left[1 + 300 \left\{ \left(\frac{\delta}{D}\right) - \frac{5}{\mathrm{Re}_g} \sqrt{\frac{2}{f_g}} \right\} \right], \tag{19}$$

where δ is the liquid film thickness, D the hydraulic diameter of the channel, and f_g the wall friction factor. f_g in the laminar region is given by the Fanning friction factor,

$$f_{g,l} = \frac{14.227}{\mathrm{Re}_g}, \tag{20}$$

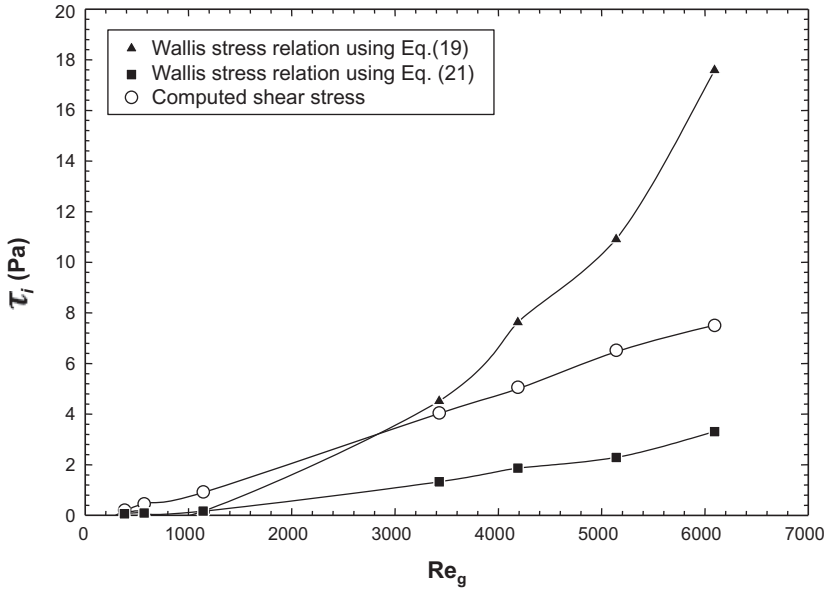

Fig. 14. Computed Domain 2 (stationary interface) nitrogen interfacial shear stress versus Re_g compared to predictions of Wallis [6].

and in the turbulent region by the Blasius friction factor,

$$f_{g,t} = \frac{0.079}{\mathrm{Re}_g^{0.25}}. \tag{21}$$

For the laminar range, the friction factor f_i in Eq. (18) is replaced by the Fanning friction factor, *i.e.*, $f_{i,l} = f_{g,l}$. Alternatively, there is also an established practice of using the Blasius wall friction factor instead of $f_{i,t}$, in Eq. (18) [49]. Fig. 14 shows the variation of the computed interfacial shear with Re_g along with predictions of the Wallis correlation using $f_{i,t}$ and $f_{g,t}$. The computed interfacial shear increases fairly linearly with increasing Re_g. The Wallis correlation using $f_{i,t}$ overpredicts the computed values for high Re_g, but shows better agreement in the laminar and transition regions. A possible explanation for the departure between the computed and Wallis results is the inability of the Wallis function, $f_{i,t}$, to account for the changing character of interfacial waves with increasing Re_g. Fig. 14 shows the Wallis shear stress relation using $f_{g,t}$ underpredicts the computed results, but provides fair agreement in slope.

Kataoka et al. [10] studied interfacial shear in the presence of interfacial waves, and proposed that the Wallis friction factor can better represent interfacial shear by incorporating the wave height in Eq. (19). Using the same rationale, the computed data are fitted according to

$$f_{i,t} = f_g\left[1 + 300\left\{0.22\left(\frac{h}{l}\right)^{-0.4}\left(\frac{\delta}{D}\right) - \frac{5}{Re_g}\sqrt{\frac{2}{f_g}}\right\}\right]. \tag{22}$$

Fig. 15(a) shows the variation of computed friction factor with Re_g, along with the Fanning correlation and curve fit for the computed turbulent region using Eq. (22). The computed f_i is arrived at by inserting the computed shear stress into Eq. (18).

From the literature, correlations for $f_{i,t}$ (for the turbulent region) were presented by Moeck [21], Fore et al. [26], Fukano and Furukawa [25], and Wongwises and Kongkiatwanitch [27], respectively, as

$$f_{i,t} = 0.005\left[1 + 1458\left\{\left(\frac{\delta}{D}\right) - \frac{5}{\mathrm{Re}_g}\sqrt{\frac{2}{f_g}}\right\}^{1.42}\right], \tag{23a}$$

$$f_{i,t} = 0.005\left[1 + 300\left\{\left(\frac{\delta}{D}\right) - \frac{5}{\mathrm{Re}_g}\sqrt{\frac{2}{f_g}} - 0.0015\right\}\right], \tag{23b}$$

$$f_{i,t} = 0.425\left(12 + \frac{v_f}{v_w}\right)^{-1.33}\left[1 + 12\left\{\left(\frac{\delta}{D}\right) - \frac{5}{\mathrm{Re}_g}\sqrt{\frac{2}{f_g}}\right\}\right]^8, \tag{23c}$$

and

$$f_{i,t} = 17.172\mathrm{Re}_g^{-0.768}\left\{\left(\frac{\delta}{D}\right) - \frac{5}{\mathrm{Re}_g}\sqrt{\frac{2}{f_g}}\right\}^{-0.253}. \tag{23d}$$

In Eq. (23c), v_w and v_g are the kinematic viscosities of water and nitrogen, respectively, at 20 °C.

Fig. 15(b) compares predictions of the above correlations with those using Eq. (19) for the turbulent region using the same δ/D ratio as the present Domain 1 configuration. For the laminar region, Eq. (20) is used in conjunction with both the present computations and all previous correlations. It is seen that [25] overpredicts the fitted data, an observation previously made in [27]. However, the fit proposed by [27] also shows significant departure in the medium flow rate range. The current fit agrees well with [14,21,26] for medium Re_g values up to about 3500, where interfacial waviness is still relatively mild, but shows slight departure from the previous correlations for higher Re_g, where waviness is more pronounced.

The present findings point to the importance of conducting detailed interfacial measurements (liquid and gas layer thicknesses) in shear driven flows, along with velocity measurements to validate computational models. Such measurements have been conducted in adiabatic falling liquid films [50,51] and provide valuable insight into both turbulence structure and interfacial waviness, albeit for relatively thick liquid layers. As discussed in [52], measurements of liquid velocity in thin layers are possible with the aid of micro-particle image velocimetry (μ-PIV), but optical requirements palace stringent limits on the size and shape of the flow channel. Given the small thickness of shear-driven liquid layers, better and more miniaturized diagnostic tools are needed to measure liquid layer thickness and characterize interfacial waves [5,53,54], as well as temperature profile across the liquid layer [55,56] in non-adiabatic systems. Similar diagnostic tools can also play a vital role in understanding more complex two-phase phenomena, such as the formation of a wavy vapor–liquid wall layer that precedes the formation of critical heat flux (CHF) in flow boiling [57–60]. A unique aspect of the waves captured in CHF studies is unusually high h/l values that exceed those of both the present

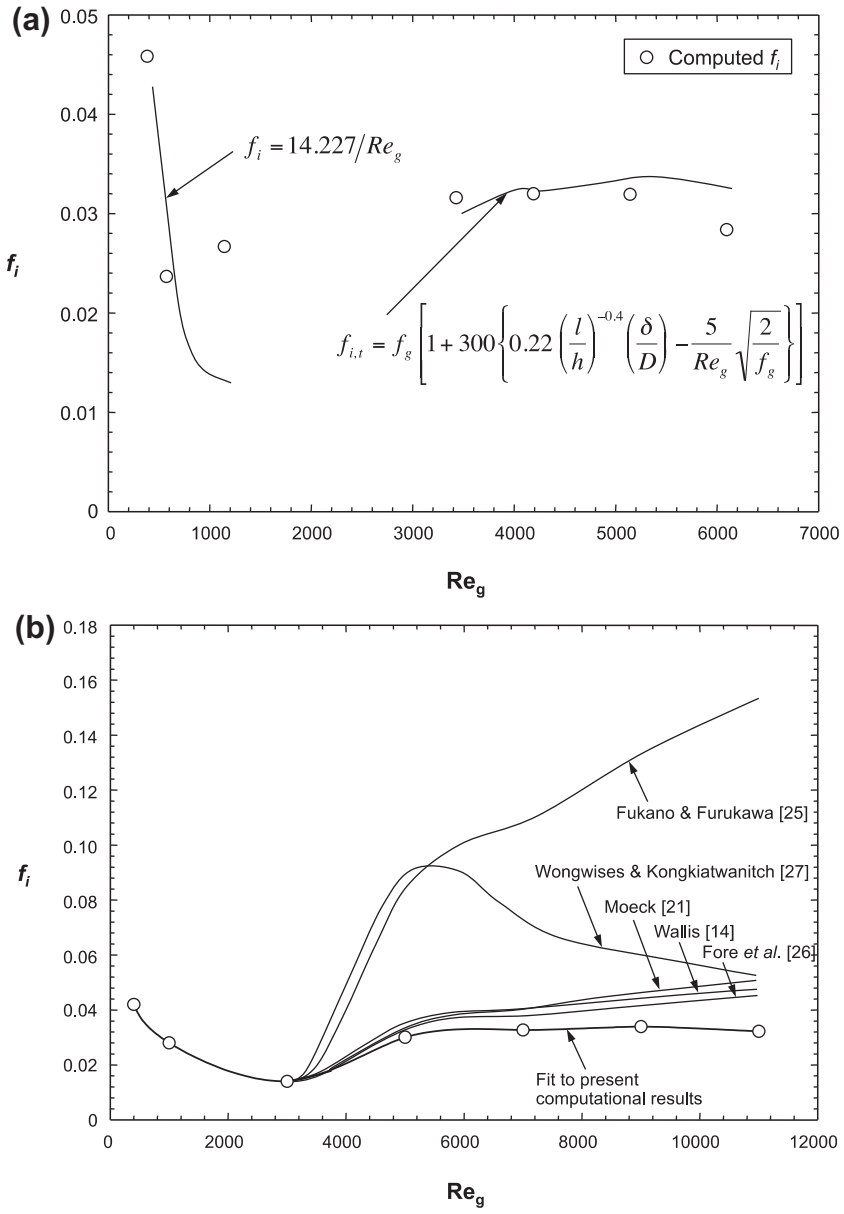

Fig. 15. (a) Variation of interfacial friction factor with nitrogen Reynolds number. (a) Curve fits to present computed results. (b) Comparison of present curve fit to previous correlations.

study and previous correlations and sinusoidal wall models. These high h/l values contribute appreciable flow separation in the wave fronts and are therefore likely to yield unusually high interfacial shear.

6. Conclusions

This study examines the fluid dynamics of the wavy interface between horizontal liquid and gas layers using water and nitrogen as working fluids. A test facility is developed to capture the interfacial behavior using high speed video. Using FLUENT, computational models are developed for two distinct domains. Domain 1 is comprised of the actual two-phase flow, and used to explore interfacial structure and eddy diffusivity. Because the mean velocity of the gas flow is much greater than that of the liquid, the liquid layer serves essentially as a solid wavy wall as far as the gas flow is concerned. Domain 2 consists of the gas flow alone, with the actual interfacial boundary computed using the first domain replaced by a wavy stationary wall. Domain 2 is employed to explore flow separation effects around solid waves, as well as the three-dimensional variations of both viscous and form drag. The computational results are fitted to a function of both the gas Reynolds number, Re_g, and ratio of wave height to wavelength. Key findings from the study are as follows.

1. A consistent ratio of liquid to gas Reynolds numbers is required to maintain a fairly horizontal interface. Flow visualization reveals increased waviness and entrainment effects with increasing flow rates of the two fluids. These trends are captured well by FLUENT, albeit with reduced interfacial intensity.
2. The interface is marred by complex three-dimensional features. The range of ratios of wave height to wavelength grows appreciably up to a liquid Reynolds number of about 5000, above which the growth is much slower.
3. Computed results using Domain 1 show turbulence at the interface is completely suppressed by surface tension, and the time-averaged eddy momentum diffusivity profile across the liquid

layer has a broader span and different slope near the interface compared to eddy diffusivity across free falling films. These differences are attributed to the influence of interfacial shear for the present gas–liquid flow.

4. Computed results using Domain 2 show the mean gas velocity is appreciably greater than that of the liquid for all cases considered. The x-velocity is highest in the advancing fronts of large waves and lowest in the rear of the same waves. This trend becomes most pronounced with increasing Re_g.
5. Velocity vector plots, contour plots and flow streamlines computed using Domain 2 show interfacial flow separation effects on the gas side beyond $Re_g = 3450$, and these effects are amplified with increasing Re_g. The gas flow impinges against the tails of large wall waves, and separates over the wave fronts. This produces form drag along the wavy interface in addition to the viscous drag.
6. The interfacial viscous and form drag components increase monotonically with increasing ratio of wave height to wavelength because of the increased frictional resistance and flow separation effects. A new relation for the interfacial friction factor is derived from the computational results, which agrees well with prior turbulent flow correlations.

Conflict of interest

None declared.

Acknowledgment

The authors are grateful for the partial support for this project from the National Aeronautics and Space Administration (NASA) under Grant no. NNX13AB01G.

References

[1] I. Mudawar, M.A. El-Masri, Momentum and heat transfer across freely-falling turbulent liquid films, Int. J. Multiphase Flow 12 (1986) 771–790.
[2] N. Mascarenhas, I. Mudawar, Investigation of eddy diffusivity and heat transfer coefficient for free-falling turbulent liquid films subjected to sensible heating, Int. J. Heat Mass Transfer 64 (2013) 647–660.
[3] N. Mascarenhas, I. Mudawar, Study of the influence of interfacial waves on heat transfer in turbulent falling films, Int. J. Heat Mass Transfer 67 (2013) 1106–1121.
[4] W. Nusselt, Die oberflächenkondensation des wasserdampfes, VDI Z. 60 (1916) 541–546.
[5] J.A. Shmerler, I. Mudawar, Local heat transfer coefficient in wavy free-falling turbulent liquid films undergoing uniform sensible heating, Int. J. Heat Mass Transfer 31 (1988) 67–77.
[6] G.B. Wallis, One-dimensional Two-phase Flow, McGraw-Hill, New York, NY, 1964.
[7] H. Lee, I. Mudawar, M.M. Hasan, Experimental and theoretical investigation of annular flow condensation in microgravity, Int. J. Heat Mass Transfer 61 (2013) 293–309.
[8] S.M. Kim, I. Mudawar, Theoretical model for annular flow condensation in rectangular micro-channels, Int. J. Heat Mass Transfer 55 (2012) 958–970.
[9] M. Ishii, N. Zuber, Drag coefficient and relative velocity in bubbly, droplet or particulate flows, AIChE J. 25 (1979) 843–855.
[10] I. Kataoka, M. Ishii, K. Mishima, Generation and size distribution of droplet in annular two-phase flow, J. Fluids Eng. 105 (1983) 230–239.
[11] M. Salvetti, R. Damiani, F. Beux, Drag prediction over steep sinusoidal wavy surfaces, Phys. Fluids 13 (2001) 2728–2731.
[12] D.E. Hartley, D.C. Roberts, A correlation of pressure drop data for two-phase annular flows in vertical channels, Nuclear research memorandum Q.6, Queen Mary College, University of London, 1961.
[13] R.S. Silver, G.B. Wallis, A simple theory for longitudinal pressure drop in the presence of lateral condensation, Proc. Inst. Mech. Eng. 180 (1965) 36–42.
[14] G.B. Wallis, Annular two-phase flow, Part 1: a simple theory, J. Basic Eng. 92 (1970) 59–72.
[15] G.B. Wallis, Annular two-phase flow, Part 2: additional effects, J. Basic Eng. 92 (1970) 73–81.
[16] W.H. Henstock, T.J. Hanratty, The interfacial drag and the height of the wall layer in annular flows, AIChE J. 22 (1976) 990–1000.
[17] J.C. Asali, T.J. Hanratty, P. Andreussi, Interfacial drag and film height for vertical annular flow, AIChE J. 31 (1985) 895–902.
[18] A. Narain, G. Yu, Q. Liu, Interfacial shear models and their required asymptotic form for annular/stratified film condensation flows in inclined channels and vertical pipes, Int. J. Heat Mass Transfer 40 (1997) 3559–3575.
[19] H.S. Mickley, Heat, mass and momentum transfer for flow over a flat plate with blowing or suction, NASA Report, NACA-TN-3208, 1954.
[20] I.G. Shekriladze, V.I. Gomelauri, Theoretical study of laminar film condensation of flowing vapor, Int. J. Heat Mass Transfer 9 (1966) 581–591.
[21] E.O. Moeck, Annular-dispersed two-phase flow and critical heat flux, Atomic Energy Canada Limited, AECL-3656, 1970, pp. 337–346.
[22] P. Andreussi, The onset of droplet entrainment in annular downward flows, AIChE J. 58 (1980) 267–270.
[23] M. Soliman, J.R. Schuster, P.J. Berenson, A general heat transfer correlation for annular flow condensation, J. Heat Transfer – Trans. ASME 90 (1986) 267–276.
[24] P.L. Spedding, N.P. Hand, Prediction of holdup and pressure loss from the two phase momentum balance for stratified type flows, in advances in gas–liquid flows, in: Proc. ASME-FED, vol. 188, Dallas, TX, 1990, pp. 73–87.
[25] T. Fukano, T. Furukawa, Prediction of the effects of liquid viscosity on interfacial shear stress and frictional pressure drop in vertical upward gas–liquid annular flow, Int. J. Multiphase Flow 24 (1998) 587–603.
[26] L.B. Fore, S.G. Beus, R.C. Bauer, Interfacial friction in gas–liquid annular flow: analogies to full and transition roughness, Int. J. Multiphase Flow 26 (2000) 1755–1769.
[27] S. Wongwises, W. Kongkiatwanitch, Interfacial friction factor in vertical upward gas–liquid annular two-phase flow, Int. Commun. Heat Mass Transfer 28 (2001) 323–336.
[28] O. Reynolds, Study of fluid motion by means of coloured bands, Nature 50 (1894) 161–164.
[29] J.O. Hinze, Turbulence, McGraw-Hill, New York, NY, 1975.
[30] D. Wilcox, Turbulence Modeling for CFD, second ed., DCW Industries Inc., La Canada, Canada, CA, 1998.
[31] ANSYS FLUENT 12.1 in Workbench User's Guide. ANSYS Inc., Canonsburg, PA, 2009.
[32] J.U. Brackbill, D.B. Kothe, C. Zemach, A continuum method for modeling surface tension, J. Comput. Phys. 100 (1992) 335–354.
[33] M. Wolfstein, The velocity and temperature distribution of one-dimensional flow with turbulence augmentation and pressure gradient, Int. J. Heat Mass Transfer 12 (1969) 301–318.
[34] H.C. Chen, V.C. Patel, Near-wall turbulence models for complex flows including separation, AIAA J. 26 (1988) 641–648.
[35] T. Jongen, Simulation and modeling of turbulent incompressible flows (Ph.D. thesis), EPF Lausanne, Lausanne, Switzerland, 1992.
[36] B. Kader, Temperature and concentration profiles in fully turbulent boundary layers, Int. J. Heat Mass Transfer 24 (1981) 1541–1544.
[37] C.W. Hirt, B.D. Nicholls, Volume of fluid (VOF) method for dynamics of free boundaries, J. Comput. Phys. 39 (1981) 201–225.
[38] S. Armsfield, R. Street, The fractional-step method for the Navier–Stokes equations on staggered grids: accuracy of three variations, J. Comput. Phys. 153 (1999) 660–665.
[39] H.M. Glaz, J.B. Bell, P. Colella, An analysis of the fractional-step method, J. Comput. Phys. 108 (1993) 51–58.
[40] W. Anderson, D.L. Bonhus, An implicit algorithm for computing turbulent flows on unstructured grids, Comput. Fluids 23 (1994) 1–21.
[41] S.V. Patankar, Numerical Heat Transfer and Fluid Flow, Hemisphere, Washington, DC, 1980.
[42] T.W. Anderson, The Statistical Analysis of Time Series, Wiley, New York, NY, 1958.
[43] B.S. Stratford, The prediction of separation of the turbulent boundary layer, J. Fluid Mech. 5 (1959) 1–16.
[44] C.G. Speziale, R. Abid, E.C. Anderson, Critical evaluation of two-equation models for near-wall turbulence, AIAA J. 30 (1992) 324–331.
[45] Y.A. Cengel, R.H. Turner, Fundamentals of Thermal-Fluids Sciences, McGraw-Hill, New York, NY, 2001.
[46] H. Schlichting, Boundary-layer Theory, McGraw-Hill, New York, NY, 1979.
[47] D.S. Henn, R.I. Sykes, Large-eddy simulation of flow over wavy surfaces, J. Fluid Mech. 383 (1999) 75–112.
[48] M.V. Salvetti, R. Damiani, F. Beux, Three-dimensional coarse large-eddy simulations of the flow above two-dimensional sinusoidal waves, Int. J. Numer. Methods Fluids 35 (2001) 617–642.
[49] R.K. Shah, A.L. London, Laminar Flow Forced Convection in Ducts: A Source Book for Compact Heat Exchanger Analytical Data, Academic Press, New York, 1978.
[50] I. Mudawar, R.A. Houpt, Mass and momentum transport in falling liquid films laminarized at relatively high Reynolds numbers, Int. J. Heat Mass Transfer 36 (1993) 3437–3448.
[51] I. Mudawar, R.A. Houpt, Measurement of mass and momentum transport in wavy-laminar falling liquid films, Int. J. Heat Mass Transfer 36 (1993) 4151–4162.
[52] W. Qu, I. Mudawar, S.-Y. Lee, S.T. Wereley, Experimental and computational investigation of flow development and pressure drop in a rectangular micro-channel, J. Electron. Packag. – Trans. ASME 128 (2006) 1–9.
[53] J.A. Shmerler, I. Mudawar, Local evaporative heat transfer coefficient in turbulent free-falling liquid films, Int. J. Heat Mass Transfer 31 (1988) 731–742.
[54] J.E. Koskie, I. Mudawar, W.G. Tiederman, Parallel-wire probes for measurement of thick liquid films, Int. J. Multiphase Flow 15 (1989) 521–530.
[55] T.H. Lyu, I. Mudawar, Statistical investigation of the relationship between interfacial waviness and sensible heat transfer to a falling liquid film, Int. J. Heat Mass Transfer 34 (1991) 1451–1464.

[56] T.H. Lyu, I. Mudawar, Determination of wave-induced fluctuations of wall temperature and convective heat transfer coefficient in the heating of a turbulent falling liquid film, Int. J. Heat Mass Transfer 34 (1991) 2521–2534.
[57] C.O. Gersey, I. Mudawar, Effects of heater length and orientation on the trigger mechanism for near-saturated flow boiling critical heat flux – I. Photographic study and statistical characterization of the near-wall interfacial features, Int. J. Heat Mass Transfer 38 (1995) 629–641.
[58] C.O. Gersey, I. Mudawar, Effects of heater length and orientation on the trigger mechanism for near-saturated flow boiling critical heat flux – II. Critical heat flux model, Int. J. Heat Mass Transfer 38 (1995) 643–654.
[59] J.C. Sturgis, I. Mudawar, Critical heat flux in a long, rectangular channel subjected to onesided heating – I. Flow visualization, Int. J. Heat Mass Transfer 42 (1999) 1835–1847.
[60] J.C. Sturgis, I. Mudawar, Critical heat flux in a long, rectangular channel subjected to onesided heating – II. Analysis of critical heat flux data, Int. J. Heat Mass Transfer 42 (1999) 1849–1862.